aerospace

Article

Design and Analysis of a Base Bleed Unit for the Drag Reduction of a High-Power Rocket Operating at Transonic Speeds

Petros Famellos [1], Athanasios Skevas [1], Asterios Koutsiadis [1], Christos Koutsouras [1] and Pericles Panagiotou [1,2,*]

[1] Laboratory of Fluid Mechanics & Turbomachinery, Department of Mechanical Engineering, Aristotle University of Thessaloniki, 54124 Thessaloniki, Greece
[2] UAV Integrated Research Center (UAV-iRC), Center for Interdisciplinary Research and Innovation (CIRI), Aristotle University of Thessaloniki, 57001 Thessaloniki, Greece
* Correspondence: peripan@auth.gr

Abstract: In the present study, a passive flow device is considered for drag reduction purposes through implementation in a transonic high-power rocket. The high-power rocket serves as a reference platform that, apart from the operating conditions, enforces several constraints in terms of available volume and placement locations. A step-by-step methodology is suggested, where the unit is initially broken down into an inlet and an outlet component. The flow field is investigated by means of computational modeling (CFD), where the Reynolds-averaged Navier–Stokes equations are solved coupled with turbulence models that vary depending on the design phase and the individual component. In the first design phase, the best alternative configuration is selected for each component by comparing mass flow rates and discharge coefficients. In the second design phase, each component is analyzed in greater detail based on the first phase results. Indicatively, the protruding inlet diffuser-type channel is converted into a protruding inlet nozzle-type channel to avoid choked flow phenomena, and a nozzle geometry is selected as the outlet amongst the other considered scenarios. The two components are eventually integrated into a common base bleed unit and a final assessment is made. The computational results are used to predict the performance and trajectory of the rocket through a well-established trajectory software. The overall methodology is validated against full-scale test flight data. The results show that the base bleed unit developed in the framework of this study yields a drag reduction of approximately 15% at transonic speeds without impacting the rocket mass and stability.

Keywords: base bleed; rocket; wake flow; drag coefficient; base drag; CFD; bell-shaped nozzle; protruding geometry

Citation: Famellos, P.; Skevas, A.; Koutsiadis, A.; Koutsouras, C.; Panagiotou, P. Design and Analysis of a Base Bleed Unit for the Drag Reduction of a High-Power Rocket Operating at Transonic Speeds. *Aerospace* **2024**, *11*, 385. https://doi.org/10.3390/aerospace11050385

Academic Editor: Sergey Leonov

Received: 31 March 2024
Revised: 3 May 2024
Accepted: 9 May 2024
Published: 12 May 2024

1. Introduction

Since the dawn of the Space Age, engineers have dedicated significant effort to designing rockets that can safely propel equipment into space [1]. In the 21st century, however, this pursuit is also combined with an ever-increasing need for better performance characteristics. A typical example is the case of the commercial space companies that aim at improving their platforms in the face of environmental and financial consequences [2].

The fact that these vehicles travel at high speeds results in high drag losses [3]. More specifically, bodies that resemble the shape of a rocket and barely reach supersonic speeds tend to suffer from a particular component of drag called base drag, which is responsible for up to 40% of the overall drag force, depending on operating conditions [4]. This component is attributed to the flow phenomena developed at the aft part of the rocket, which is usually blunt-shaped. When the engines are cut off during the coasting phase, the flow separates and the wake is dominated by vortices that create a low-pressure area, which in turn results in an increase in pressure drag [5].

Due to these high losses, the need for aerodynamically optimized rocket-like vehicles calls for dedicated research on drag reduction techniques and devices. Several studies investigate both passive and active devices (units) that manipulate the flow and shift the vortices downstream so that their interaction with the wake is minimized, thus altering the pressure distribution and reducing base drag. A typical example can be found in Danberg et al. [6], who studied the predicted flight performance of projectiles with an active base bleed unit. The results showed a 23% increase in terms of the range of the supersonic flow regime, as well as a 17% increase in operation at the flight ceiling. The drag reduction was not the main focus of the study and, as such, this metric was not quantified. In another active flow control-related study, Choi et al. [7] studied the base drag reduction potential of an active base bleed unit, simulating the combustion process in the additional grain, and reported a 10% drag reduction on a projectile configuration. Abou-Elela et al. [8] performed ballistic analysis of a projectile with an active base bleed unit and found a decrease in the drag coefficient across multiple free-stream flows.

As shown in these studies, active base bleed units have a considerable potential in reducing base drag. However, active base bleed units require a secondary propellant to operate, which in turn results in a weight increase [9]. This weight penalty can have a negative effect on the performance of a rocket that has been designed to fulfil a specific mission (apogee, distance, etc.). Additionally, it must be noted that as the active base bleed units are installed at the bottom of the rocket, this weight penalty is concentrated aft of the rocket center of gravity, impacting the stability of the rocket in a negative way. Apart from the weight penalty, these active base bleed units require a dedicated volume inside the body tube, which is scarce for a rocket with constrained dimensions. Finally, active control devices involve electronics and automated procedures for their operation, which further adds to the complexity of the system.

As an alternative to their active counterparts, passive flow control devices have also been investigated, with emphasis on passive base bleed units. More specifically, Paul et al. [10] implemented base bleed technology on a shell projectile, with a bleed hole inlet configuration combined with a boat tail. The study showed a 75% decrease in base drag in supersonic flow regions. However, it should be noted that the inward geometry configuration utilized is rarely implemented on a rocket due to high-temperature exhaust gases that may deform the outlet channels and thus demands a higher-grade material that can withstand the generated heat. In another related study [11], the effect of passive base bleed units in vortex shedding was investigated, proving that passive devices could be used as an alternative approach. This study is experimental and focused on the quantification of the vortex shedding using the Strouhal number as a key parameter, thus serving as an important indicator of how the outlets should be designed and evaluated. In another related paper [12], base bleed cavities were studied among other flow arrangement techniques for base drag reduction at supersonic speeds, broadening the velocity range at which our design could potentially operate. The results showed a 5% drag decrease.

As a general comment, previous studies cover the topic of base bleed unit implementation on projectiles and bullets. To the best of our knowledge, no study has been published specifically for rocket vehicles. However, the drag reduction potential presented in the existing literature, combined with the various methods developed from the corresponding researchers over the years, along with the fact that projectiles and rockets share general characteristics to some extent, serves as the motivation for a new, unique design study to be conducted for a flow control device on a rocket vehicle.

In the current paper, the design, fine-tuning and implementation of a flow control device are presented for a high-power rocket, which serves as the reference platform. Note that the reference platform specifications are not arbitrarily selected. It is a prototype high-power rocket designed and developed from scratch to comply with the guidelines set by the European Rocketry Challenge (EuRoC) International competition, supported by the European Space Agency and the Portugal Space Agency. Developed under the callsign "Eclipse," its goal is to reach an apogee of 3 [km] as accurately as possible, with a trajectory software documenting the key parameters for flight validation. Based on these high-level mission requirements, the design engineers conduct the sizing of the rocket and calculate its specifications related to performance, structures and aerodynamics. In the work at hand, the authors emphasize on the latter, i.e., the design of a base bleed unit that can enhance the aerodynamics of the Eclipse.

Figure 1 shows the key geometrical specifications of the reference platform, along with an indicative, baseline base bleed unit configuration. It must be noted at this point that, before the fine-tuning analyses kicked off, the vehicle design was largely concluded, thus enforcing several key constraints and challenges and leaving little-to-no room for adjustments to its general layout. This is a consideration that sets apart the current study from previously published articles, since the implementation of the base bleed unit on a rocket configuration must consider the added complexity that the system architecture introduces. For example, the rocket motor and fins enforce additional spatial constraints, which have an impact on both the available positioning space for the channels and their maximum dimensions. This means that the drag reduction and, in turn, the base bleed fine-tuning must be conducted at a minimal weight and with volume penalties to avoid major redesign loops. Moreover, given that, as discussed above, active base bleed units require the addition of secondary propellants (grains) and control parts, a passive approach is eventually selected. The fine-tuning conditions correspond to a free-stream flow velocity range up to the transonic regime, where the losses of the rocket maximize during flight without interfering with its stability.

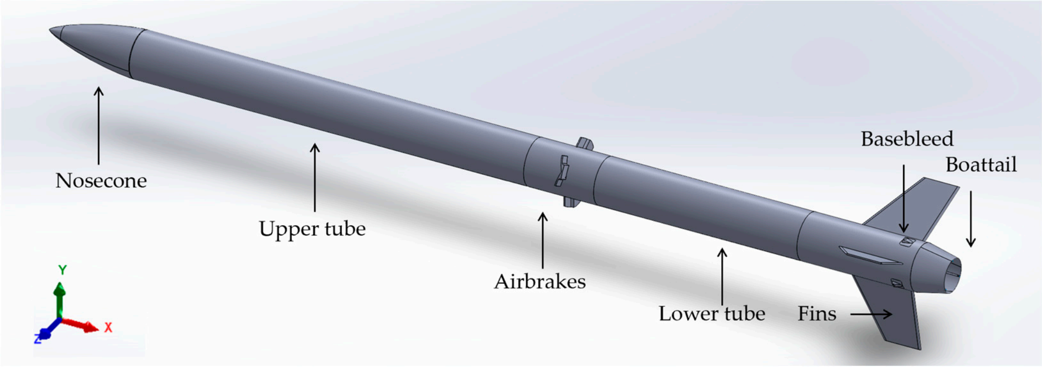

Figure 1. Reference platform (Eclipse rocket).

Summing up, the key objectives and novelties of this study are as follows:

(1) Present a complete, from-conceptualization-to-implementation methodology that can be utilized by future researchers in the field. The authors not only provide a specific set of results but go through a step-by-step presentation of their methodology and considerations, opening the way for future design studies on passive flow control devices to be conducted on rockets by researchers who investigate means of reducing drag and, thus, fuel consumption. Also, the fact that the rocket and thus the device were tested under the supervision of a well-organized and directed competition serves as proof of a mandatory protocol for evaluation and documentation.

(2) Propose a reliable, high-fidelity computational fluid dynamics-based (CFD-based) approach to be used with the design methodology of the first objective. This is another key point of the current work, since the analysis methodology is validated against a full-scale field test conducted according to the EuRoC guidelines, made from a specific launch site under specific, reproduceable conditions.

(3) Investigate a flow control device and fine-tune its parameters to reduce the drag of a rocket vehicle that operates up to transonic speeds. Emphasis is placed on the passive base bleed system, considering a wide range of operating conditions along with the limitations in weight and volume imposed by the reference platform. The resulting configuration is unique, as it consists of a protruding geometry inlet and a nozzle-type outlet. To the best of our knowledge, these characteristics have not been reported in other base bleed studies, where the common practice is to employ angled holes (bleed

holes) in the body of the platform, as well as a straight or angled pipe outlet, with the pipe diameter, however, remaining constant. This is an indication that the boundary conditions of the current design study, i.e., the operating conditions and limitations, lead to a different design philosophy, tailored to the needs of the high-power reference platform.

Concerning the structure of the paper, Section 2 starts by presenting the details of the specifications of the base bleed reference platform and its specific mission requirements (e.g., apogee). The corresponding placement considerations and design process are then discussed. The computational methodology is analyzed, accompanied by the rationale behind each key choice. The evolution of the design as well as the results of the design procedure are presented in Section 3, along with the CFD modeling results. The comparison against the flight data is also analyzed for validation purposes. This section also includes a presentation of the tool used to calculate the trajectory of the rocket and predict its performance at the EuRoC (Rocket.py). Finally, a more thorough discussion is provided in Section 4, followed by Sections 5 and 6, which briefly summarize the key conclusions and suggestions for future work.

2. Materials and Methods

2.1. The Eclipse Rocket Reference Platform

2.1.1. Mission Requirements

The reference platform for the current study is a high-power rocket configuration, whose mission is to reach a specific apogee under the conditions of the EuRoC competition. More specifically, its mission profile is to takeoff from a stable ground platform, rise to an apogee of 3000 m, deliver the payload via airdrop, and safely glide back to the ground by a system of parachutes (Figure 2). The rest of the Eclipse requirements are summed up in Table 1.

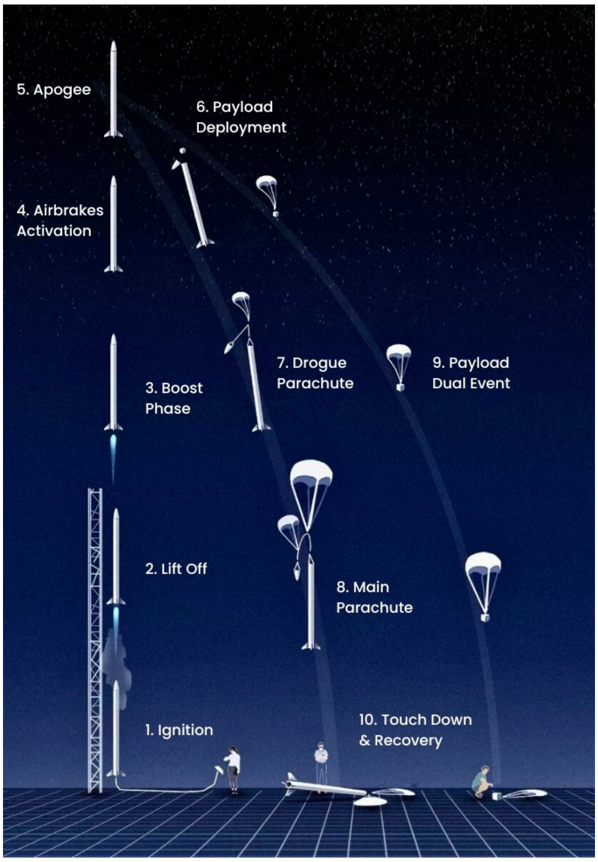

Figure 2. Mission profile schematic.

Table 1. Mission profile requirements.

Flight Requirements	Avionics Requirements	Other Requirements
Cargo weight < 4 [kg]	Automated ejection at apogee, guided descent	Use of lightweight aluminum alloys
Apogee 3000 [m]	Automatic control precision systems	Ambient temperature
Maximum speed M = 0.87	Redundant flight control system	Maintain structural integrity
Stability (1.5,5) [cal *]	Real time flight data monitoring	Minimum stability off-rail
Take-off point at Santa Margarida military camp	-	-
Take-off altitude at h_0 = 165 [m]	-	-
Maximum wind speed < 9 [m/s]	-	-

* cal: Stability variable of rockets regarding the relative location of the center of mass and the center of pressure measured in reference to rocket's body largest diameter [13].

2.1.2. Overall Platform Specifications

The Eclipse layout is a high-power solid motor rocket, with the payload bay located at the upper tube and the engine and control departments inside the lower tube. The dimensions of the main body, i.e., diameter and length, are determined by EuRoC demands, which dictate the available volume for installing the avionics and all other subsystems (components) required for operating the rocket nominally. To maximize aerodynamic stability, the heaviest components are placed near the nosecone of the rocket to shift the center of mass forward. Meanwhile, a set of three airfoil fins has also been designed and installed at the rear of the rocket. Even though the base bleed unit has not yet been designed at this point, it must be noted that its mass must be as low as possible, so that the center of mass is not shifted afterwards. The overall specifications of the Eclipse at the end of its conceptual design are presented in Table 2.

Table 2. Eclipse's structural specifications.

Key Eclipse Specifications	
Take-off weight [kg]	31.9
Fuel weight [kg]	7.5
Cargo weight [kg]	4
Length [m]	2.96
Diameter [m]	0.149
Fin root chord [m]	0.21
Fin tip chord [m]	0.12
Sweep angle [deg]	60.6
Fin height [m]	0.205
Ascend time to apogee [s]	24
Maximum speed [-]	Mach 0.856 *
Altitude at maximum speed [m]	200
Minimum stability [cal **]	2.73

* Speed of sound calculated at sea level. ** cal: Stability variable of rockets, regarding the relative location of the center of mass and the center of pressure measured in References to rocket's body largest diameter [13].

2.2. CFD Methodology

As the rocket is designed to operate up to transonic speeds, the methods for the analytical calculation of the aerodynamic coefficients are insufficient [3]. Instead, high-fidelity CFD modeling is used, coupled with experimental data for validation purposes. The modeling is conducted using ANSYS FLUENT, version 2022R2 commercial software as the solver, the BETA CAE Systems ANSA v23.0.1 for pre-processing, and BETA CAE Systems META v.23.0.1 for post-processing. The CFD methodology involves both two-dimensional (2D) and three-dimensional (3D) simulations. The combination of two-dimensional and three-dimensional CFD analysis is used as certain designs displayed symmetric geometrical properties, which allows for less-demanding methods from a computational resource's perspective. Both pre- and post-processing are conducted on a desktop computer with 32GB RAM, 2.7 GHz AMD Ryzen 7 68000U Processor and a 64-bit operating system. Solving was conducted on the High-Performance Cluster of the Aristotle University of Thessaloniki with an Intel Xeon E5-2630 v4 Processor and 20 CPU Cores. The modeling approach is selected based on the corresponding literature [14,15], as are the parameters for each of the analysis. The Reynolds-averaged Navier–Stokes (RANS) equations are solved, coupled with the energy equation and a two-equation turbulence model, and a steady-state approach is used. The free-stream flow air is considered as an ideal gas, while low Reynolds models are used for the external modeling (inlets) and high Reynolds models are used for the internal modeling (outlets). A more detailed presentation of the model parameters is provided below and summarized in Table 3.

Table 3. CFD parameters.

CFD Parameters	Phase A–Inlets	Phase B–Inlets	Phase A–Outlets	Phase B–Outlets	Integration and Validation
Turbulence model	k-ε Realizable	k-ω SST	k-ε Realizable	k-ε Realizable	k-ω SST
Discretization scheme	First order	Second order	Second order	Second order	First order
Element number	2,500,000	10,000,000	500,000	500,000	24,000,000
Control volume inlet conditions	Velocity Inlet	Velocity Inlet	Velocity Inlet	Velocity Inlet	Velocity Inlet
Control volume outlet conditions	Pressure Outlet	Pressure Outlet	Pressure Outlet	Pressure Outlet	Pressure Outlet
y^+ on the wall	30	1	30	30	1
Mach number	0.6–0.9	0.6–0.9	0.17–0.32	0.17–0.32	0.3–0.9
CFL	5	5	1	1	1

- Base bleed inlet investigation: For the inlet component, the k-ε realizable turbulence model is used in 2D CFD simulations, as the aim is mainly to determine any potential fundamental problems in channel performance, i.e., the presence or not of choked flow phenomena. In the 3D simulations, the k-ω SST turbulence model is used, as the interaction of the component with free-stream outer flow is the main phenomenon investigated. The turbulence inlet conditions, meaning the inlet values of the turbulent kinetic energy (k), turbulence dissipation rate (epsilon), and the specific dissipation rate (omega), are calculated as a function of the free-stream velocity and the reference length of the vehicle, as derived from Spalart et al. [16] and shown in Equations (1)–(3).

$$k = 10^{-6}U^2 \tag{1}$$

$$\omega = 0.1U/(L_c) \tag{2}$$

$$\varepsilon = 0.09^{\frac{3}{4}}\frac{k^{\frac{3}{2}}}{l} \text{ where } l = 0.038d_h \tag{3}$$

Note that U is the free-stream flow velocity, L_c is the characteristic length, and l is the mean diameter of the inner channel. The control volume inlet and outlet boundary conditions are set as a function of the free-stream velocity (velocity inlet); in [14], they also used the free-stream temperature, and in [17], they used the free-stream pressure (pressure outlet). The control volume size for each base bleed inlet analysis is a rectangle whose length is 17 times the characteristic length of the inlet; its height is 14 times the characteristic length of the inlet, and its width is 14 times the characteristic length of the inlet. Finally, the size of the grid is determined by the target y^+. That is, the resulting grid is made up of approximately 10 million cells, while the computed values of the wall y^+ do not exceed 1.

- Base bleed outlet investigation: The outlet is treated differently from the inlet component as the priority now shifts towards calculating the mixing flow of the jet flow [18]. A high Reynolds model is used as the importance of near-wall functions is negligible. More specifically, the K-e realizable model is used as it is preferred for jet flows that include non-rotational fluid areas. The control volume inlet and outlet boundary conditions were directly taken from the previously conducted base bleed inlet analysis as the outflow conditions of the base bleed inlet, and they practically match the inflow conditions of the base bleed outlet. A control volume velocity inlet boundary condition is selected with velocities in a range of 0.17–0.32 M, as the base bleed inlet analysis results indicated, and a control volume pressure outlet boundary with ambient pressure was also used, as is the case in the literature [14–17]. Again, the control volume size for each base bleed outlet analysis is a cube whose length is 17 times the characteristic length of the base bleed outlet, the height is 14 times the characteristic length of the base bleed outlet, and the width is 14 times the characteristic length of the base bleed outlet. Finally, no grid dependency study is conducted as the design period was limited by timeline restrictions, and y^+ convergence was deemed satisfactory. The grid is comprised of 500 thousand elements that provide enough resolution for the solver to reach the targeted value of y^+, which is set to 30.
- Synergetic investigation: the k-ω SST turbulence model is used for the same reasons as in the base bleed inlet section. The combination of low and high Reynolds models that can simulate the turbulence by using wall functions and the transport equation when needed constitutes a very compelling aspect of the model. The control volume inlet values of the turbulent kinetic energy (k) and the specific dissipation rate (omega) are inputted as a function of the free-stream velocity and the reference length of the vehicle, derived again from [16]. The control volume inlet and outlet boundary conditions are chosen as a function of the free-stream velocity (velocity inlet), the free-stream temperature, and the free-stream pressure (pressure outlet). Velocities from Mach 0.3 to 0.9 are used to capture the vast majority of the velocity range of the rocket. Additionally, a simulation with the maximum velocity of 193 m/s that reached an atmospheric pressure at an apogee of 2300 m is run for validation purposes, to match the conditions of the flight test. The control volume size for each analysis is a cube whose length is 24 times the characteristic length of the outlet, whose height is 20 times the characteristic length of the rocket, and whose width is 20 times the characteristic length of the rocket. The target y^+ is set to 1, and the corresponding grid consists of 24 million elements.

As a general comment, the grid size is selected so that the values of y^+ align with the literature guidelines [14], thus ensuring the proper modeling of the flow phenomena inside the boundary layer. Moreover, it should be noted at this point that higher accuracy is feasible with more advanced turbulence models or a Large Eddy Simulation (LES) approach. However, time constraints and computational resource limitations did not allow for such an approach. Also, given that the scope of the work is mainly to conduct an engineering design study, the authors emphasized comparing the alternative configurations on “equal terms”, i.e., using a common modeling approach for each component of the base bleed unit. As a final note, the results of the full-scale flight test, which is conducted using the same boundary conditions as those shown for the complete configuration, show that the CFD methodology is reliable, at least for meeting the objectives of the current study, i.e., coming up with a well-tuned base bleed configuration. Table 3 summarizes some key CFD parameters for the different design phases and components.

2.3. Base Bleed Unit Placement

The base bleed unit design space is defined by the following:

- Structural and volume limitations (radial). As discussed above, the base bleed unit must not intervene with the components and motor layout. Therefore, a radial distance of 15 mm is available, measured from the inner radius of the tube. The innermost structure that defines the aforementioned value is the engine's heat retainer and cover tube, and the outermost is the internal layer of the rocket's lower tube, as can be seen in Figures 3 and 4. Different colors are used in Figures 3 and 4 to indicate the presence of different components, i.e., the engine grains (pink), the fins (red), the engine nozzle (light blue), the fins locking mechanism (dark blue), the engine heat retainer (yellow) and the base bleed unit (brown).
- Flow turbulence (longitudinal). To keep the inlet clean of highly turbulent flow, the authors were tasked with the determination of high-turbulence areas that should be avoided. These results showed that the main part of the rocket that introduces turbulence to the incoming flow is the launch rail buttons. The latter are located 2 m from the nosecone of the rocket in the longitudinal direction and extend for 0.1 m more in the longitudinal direction (Figure 5). Hence, the base bleed inlet must be located at least 0.1 m further downstream from the launch rail buttons.
- Structures interfering from the inside of the tube: Towards the rear of the rocket, the base bleed unit placement is constrained by the presence of the boat-tail (Figure 4), which is located 0.68 m from the launch rail buttons. Therefore, a total distance of 0.58 m is available for base bleed unit placement in the longitudinal direction.
- Shock waves (azimuthial): At the maximum expected flight speed, shock waves are predicted to form around areas of adverse pressure gradients. For this particular reference, platform shock waves appear only at the nosecone and the rear of the rocket, where the fins create attached shock waves as the rocket enters the transonic flight regime (Figure 6). Note that the boundaries of the isosurface marked in yellow are defined by a Mach number equal to 1. The nosecone shock waves do not interact with the flow at the rear of the rocket. On the contrary, an area near the interface between the lower tube of the rocket and the boat-tail should be examined in more detail as a detailed representation must be provided by high-fidelity analysis.

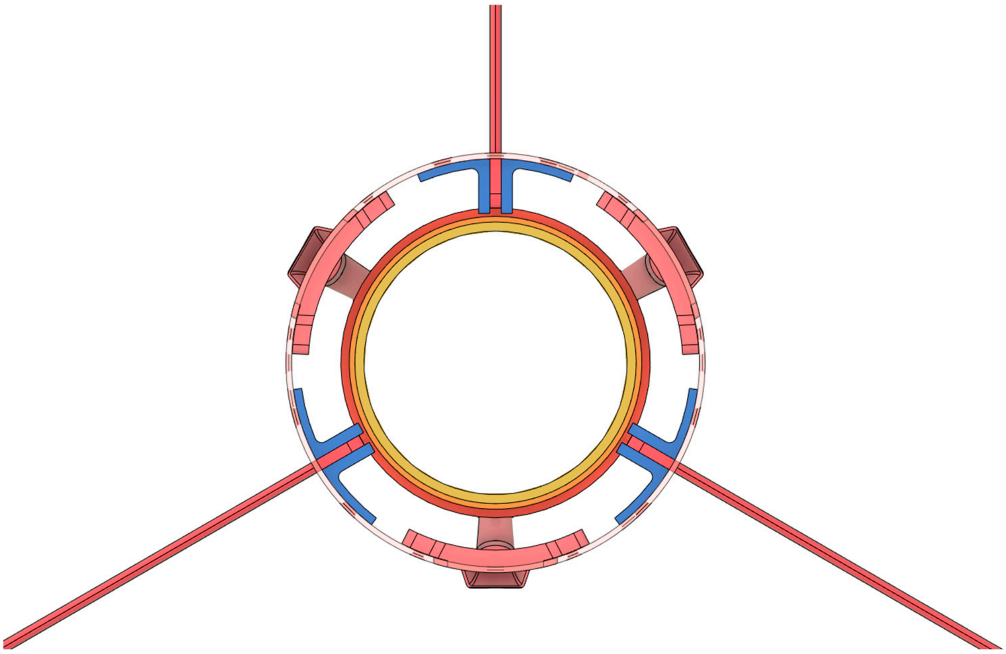

Figure 3. Rear view of the rocket at the location of the unit.

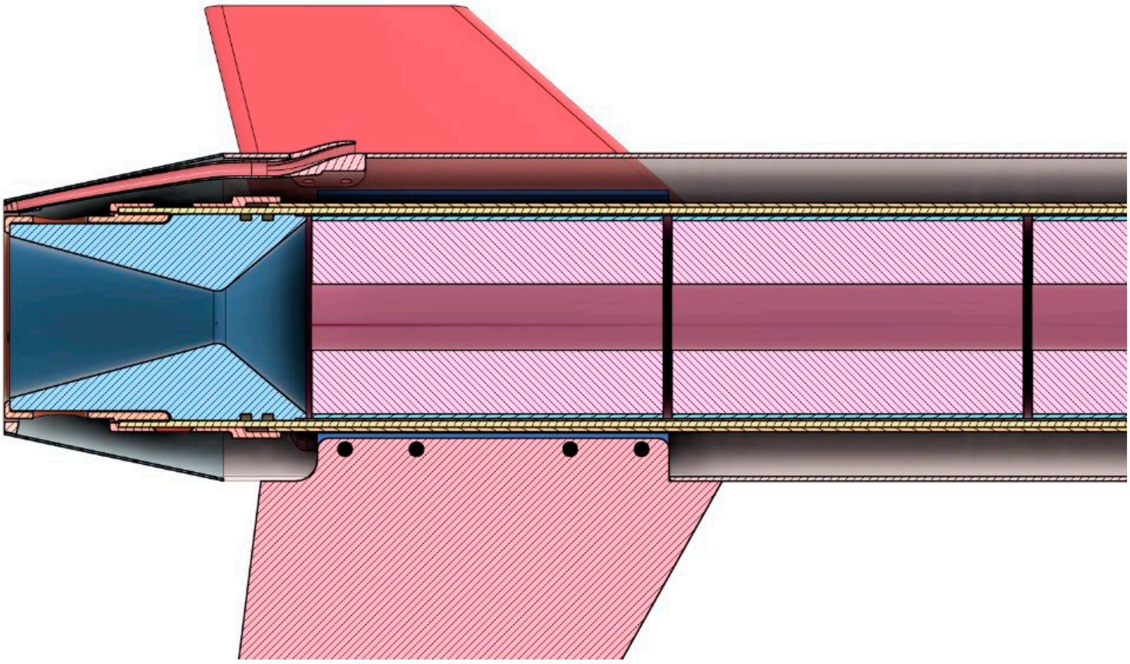

Figure 4. Side view of the rocket in the location of the unit.

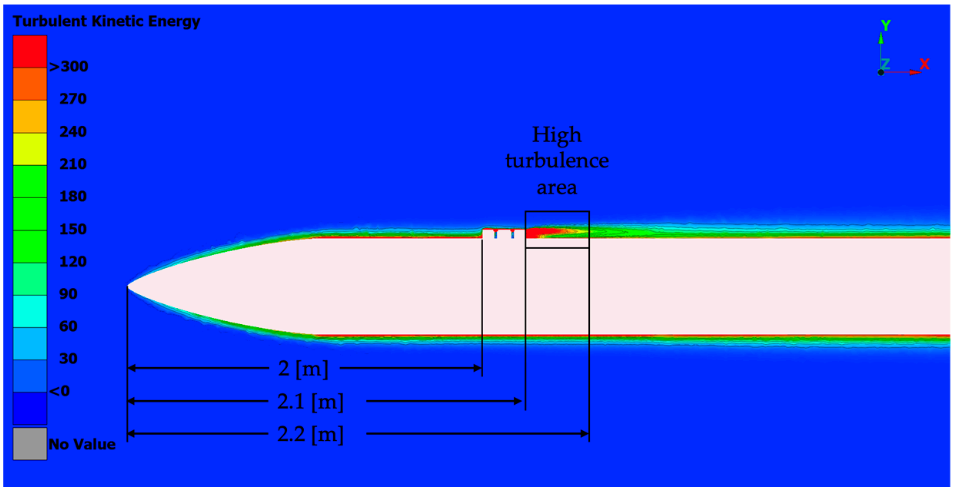

Figure 5. Reference platform turbulence in available placement area.

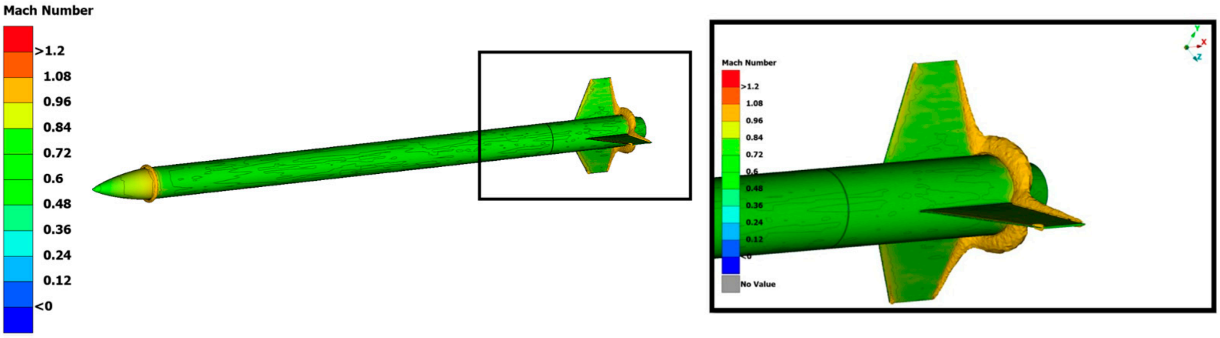

Figure 6. Shock waves across the reference platform (**left**) and shock waves at area of interest (**right**).

2.4. Base Bleed Configuration Parameters Definition and CAD Representation

To carry out the CFD computations, a 3D CAD model is first developed to ensure that every part of the configuration is properly drawn. The external cylindrical shape of the rocket dictates that the line of intersection between the tube and the inlets will follow the same pattern. Figure 7 is an indicative detailed drawing of the frontal view of the inlet section, where the key dimensions are shown, as generated from the 3D CAD model. The dimensions for Figure 7 are shown in Table 4 below.

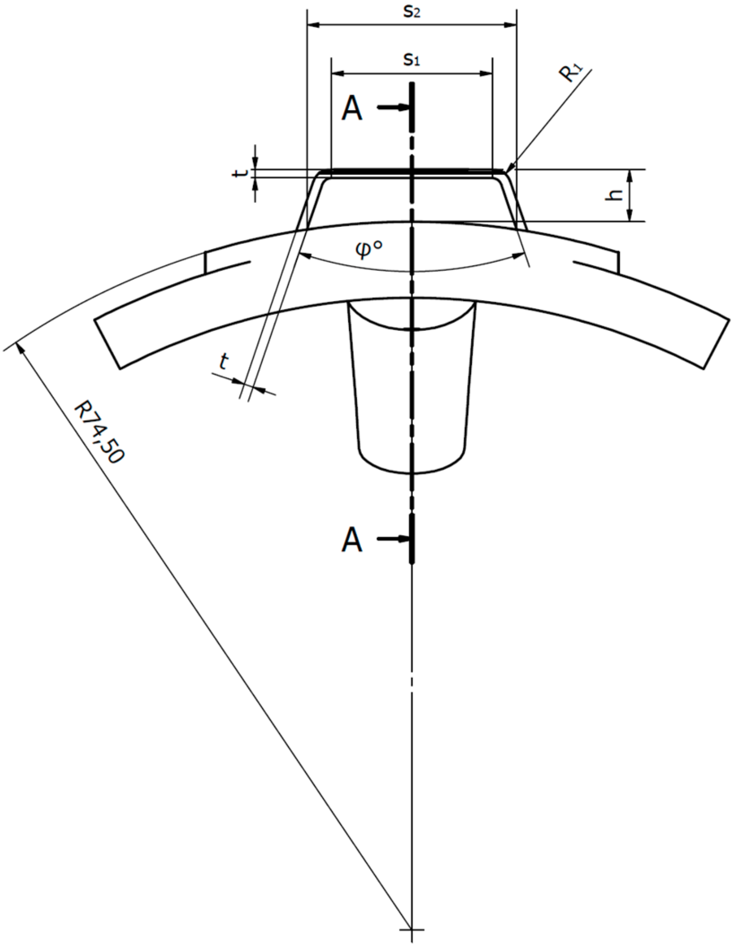

Figure 7. Base bleed unit frontal view.

Table 4. Dimensions for Figure 7 base bleed unit.

Dimension	Value
h	4.6 mm
t	1 mm
S_1	16.9 mm
S_2	22 mm
R_1	2.2 mm
φ	37.6°

2.5. Design Process Overview

The unit is broken down into two distinct components, i.e., the inlet and the outlet.

A flowchart of the design process and performance estimation procedure can be seen in Figure 8, with each design phase being analytically explained below.

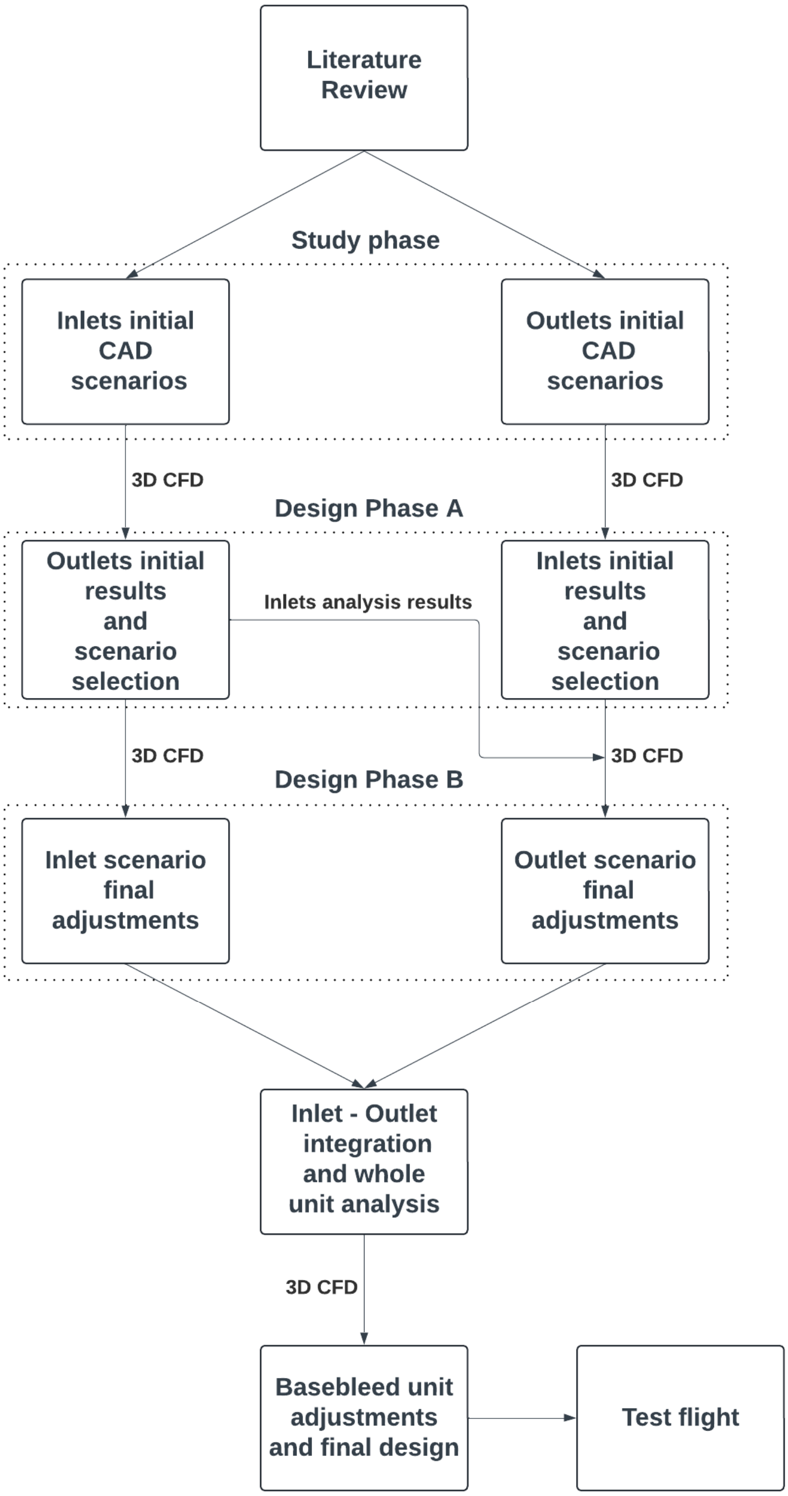

Figure 8. Base bleed unit flowchart of design phases.

2.5.1. Study Phase

In this design phase, bibliographic research is conducted to derive designs of the same usage (i.e., base bleed units), as well as designs relevant to the unit (i.e., transonic inlets, diffusers, nozzles, etc.).

Inlet Initial CAD Scenarios

In the study phase for the apparatus's inlet configurations, two distinct design scenarios are evaluated: (i) the integration of angled circular holes in the rocket's body tube, referred to as "bleed holes", and (ii) the implementation of geometries protruding from the rocket's body, named "protruding geometries". Earlier research and implementation on the topic of base bleeds saw only bleed hole configurations being used [10]. The introduction of a protruding geometry is introduced in the current study to significantly enhance air mass flow, thereby improving efficiency. More specifically, 3 mm and 6 mm bleed holes with a fifteen-degree angle are tested, as seen in [10]. A novel protruding inlet design is created inspired by [19] and scaled to fit the rocket's dimensions.

Outlet Design Considerations

By reviewing a bibliography regarding various shaped outlets, two different outlet designs for the base bleed unit are examined: (a) a bell-shaped nozzle outlet and (b) a straight circular outlet. These designs are the most compatible with the rocket's space limitations and are those with the higher expectations on performance [20]. The evaluation of these designs is based on their calculated discharge coefficients.

2.5.2. Design Phase A

In this phase, the results from CFD analysis on study phase designs are examined, and the evaluation of the designs according to their metrics takes place, leading to one design for each of the two parts. The results for each part and the evaluation process are briefly described below with more details on metrics and results.

Inlets Initial Results and Scenarios Selections

Phase A is concluded by calculating mass flow at each design part for different velocities, as shown in the Inlet Phase A results. Based on mass flow coefficient values, the protruding inlet is selected as the preferable configuration. Calculated values for mass flow coefficient for each inlet scenario are presented in Table 5. A depiction of the protruding geometry inlet design is also presented in Figure 9.

Table 5. Mass flow coefficients at different velocities for the three inlet scenarios.

3 mm Bleed Hole		**6 mm Bleed Hole**		**Protruding Geometry**	
Velocity [m/s]	**Mass Flow Coefficient**	**Velocity [m/s]**	**Mass Flow Coefficient**	**Velocity [m/s]**	**Mass Flow Coefficient**
204	0.072	204	0.1	204	0.43
238	0.072	238	0.1	238	0.43
272	0.071	272	0.09	272	0.43
309	0.07	309	0.09	309	0.43

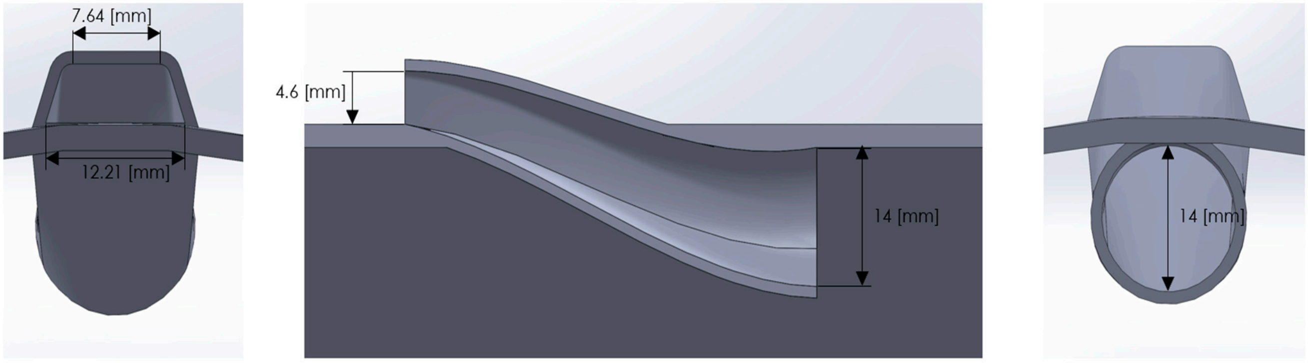

Figure 9. Initial protruding design.

Figure 9 shows the initial protruding design. From the dimensions and the photos, it can be concluded that the channel is a diffuser-type channel as the area at the trapezoidal face, where the air is ingested, is smaller than the area in the circular face.

Outlet Design Selection

After evaluating the results of CFD analysis and the calculated discharge coefficient on both these designs, it is concluded that the superior design for the outlet was the bell-shaped nozzle, as can be seen in Table 6. This design showed a higher discharge coefficient, resulting in its selection for the unit.

Table 6. Discharge coefficients at different entry velocities for the two possible outlet designs.

Straight Outlet		**Bell-Shaped Outlet**	
Entry Velocity [m/s]	**Discharge Coefficient**	**Entry Velocity [m/s]**	**Discharge Coefficient**
60	0.304	60	0.663
70	0.353	70	0.754
80	0.404	80	0.845
90	0.455	90	0.910
100	0.501	100	0.952
110	0.541	110	0.988

2.5.3. Design Phase B

In this phase, the results from CFD analysis are evaluated and the adjustments of each part design according to the results are conducted, leading to the final design of each part. The results for each part and the evaluation process are briefly described below with more details on metrics and results.

Inlets: Protruding Geometry Scenario Adjustments

To conclude the inlet design, the protruding geometry needs to be adjusted to eliminate choked flow phenomena after free-stream flow entry into the channel. This is attributed to the channel's diffuser-type geometry, with its surface area largening axially towards the rocket's base. The transition of the channel to a nozzle-type channel configuration with a diminishing cross-sectional area axially is selected based on fluid dynamics theory [3]. This adjustment is employed on the part connecting inlets and outlets as well.

Outlets: Bell-Shaped Nozzle Outlet Scenario Adjustments

The final adjustments to the outlets part include a rescaling of the geometry, a slight angle given to match the boat-tail angle, and an extension to the geometry to match the cross-section of the rockets base.

2.6. Metrics Definition

The metrics used to evaluate the performance of each separate part, i.e., the inlet and outlet parts, as well as the performance of the whole configuration, are given in Table 7:

Table 7. Performance metrics.

Inlet Part Performance Metrics	**Outlet Part Performance Metrics**	**Overall Unit Performance Metrics**
Rate of mass flow coefficient	Discharge coefficient	Overall drag coefficient Lambda 2 criterion

Performance Metrics for Each Design Part and Overall Unit

For the inlet part, mass flow is the most important factor when it comes to base bleed efficiency, as the part's role is to successfully ingest the maximum amount of free-stream flow into the channel. The non-dimensional coefficient used is rate of mass flow coefficient C_q, derived from [11] and calculated as $\dot{m}\ /\rho_\infty V_\infty A_{reff}$, where ρ_∞ and V_∞ represent free-stream density and velocity, respectively, and A_{reff} represents the area surface that the air comes through. Local drag coefficient C_D is also measured to evaluate the overall drag increase induced by inlets.

As for the outlet part, the metric used to evaluate the part's efficiency is the discharge coefficient, derived from [21] and defined as shown in Equation (4).

$$C_{dis} = \frac{\dot{M}_{actual}}{\dot{M}_{isen}} = \frac{\iint_{A_2} \rho(\overline{u}\,\overline{n})dA}{\dot{M}_{isen}} \tag{4}$$

Note that A_2 is the cross-sectional area of the outlet at the exit and $\dot{M}_{isen}$ is calculated as shown in Equation (5).

$$A_2 P_1 \left[\frac{2\gamma}{\gamma - 1} \frac{M_w}{R_g T_1} \left[\left(\frac{P_3}{P_1} \right)^{2/\gamma} - \left(\frac{P_3}{P_1} \right)^{(\gamma+1)/\gamma} \right] \right]^{1/2} \tag{5}$$

Note that P_1 and T_1 are the pressure and temperature of the outlet's entry, P_3 is pressure downstream of the outlet's exit, γ is the isentropic exponent and $M_W\ and\ R_g$ are the molecular weight of air and universal gas constant, respectively. This equation emerges from [21] in the scenario where pressure ratio $\frac{P_3}{P_1}$ is lower than $\frac{P_2}{P_1}$.

The actual mass flow $\dot{M}_{actual}$ is calculated from the CFD results by obtaining the density weighted average at the outlet's entry and at the outlet's exit, as well as the weighted average velocity at the same areas multiplied by the area. The ideal isentropic $\dot{M}_{isen}$ flow used to calculate the ideal flow is calculated using Equation (2), as indicated by [15]. The assumptions made in this calculation are:

- Isentropic flow (frictionless).
- Steady-state flow.
- No chemical reactions.
- Negligible velocity of approach.
- The velocity and fluid properties are constant across sections normal to the flow (i.e., no radial gradients).
- The gas entering and exiting the nozzle has only an axial component to the velocity vector.

The base bleed unit's efficiency is primarily dictated by drag coefficient C_D. To further evaluate its efficiency, the lambda 2 criterion is deployed to identify wake flow vortices and, thus, compare wake regions affected from the base bleed with those unaffected, as the unit's function relies on the aforementioned vortex shedding phenomenon. As mentioned by Dong et al. [22], the λ-2 criterion is defined. The base bleed unit's efficiency is primarily dictated by drag coefficient C_D. To further evaluate its efficiency, the lambda 2 criterion is deployed to identify wake flow vortices and, thus, compare wake regions affected from base bleed with those unaffected, as the unit's function relies on the aforementioned vortex shedding phenomenon. As mentioned by Dong et al. [22], the λ-2 criterion is defined so that S denotes the rate-of-strain tensor and Ω denotes the rate-of-rotation tensor. By neglecting the unsteady irrotational straining and viscous effects, the symmetric part of the gradient of the incompressible Navier–Stokes equation can be expressed as shown in Equation (6).

$$S^2 + \Omega^2 = -\frac{1}{\rho} \cdot \nabla^2 P \tag{6}$$

Hence, $S^2 + \Omega^2$ determines the existence of a local pressure minimum. This matrix of $\nabla^2 P$ is real and symmetric and thus has exactly three real eigenvalues. These eigenvalues are computed and sorted in the decreasing order: $\lambda_1 \leq \lambda_2 \leq \lambda_3$. A vortex is then defined as a connected region where two of the eigenvalues are negative, which is equivalent to the condition $\lambda_2 < 0$. The eigenvalues of S^2 and Ω^2 are related as described in Equation (7).

$$Q = \frac{1}{2} tr\left(S^2 + \Omega^2\right) = -\frac{1}{2}(\lambda_1 + \lambda_2 + \lambda_3) \tag{7}$$

It can be shown that while the Q method measures the excess of rotation rate over the strain rate magnitude in all directions, the λ_2 method looks for this excess only on a specific plane. For visualization, since for every grid point a corresponding λ_2 value can be computed, the λ_2 method transforms the original vector field into a scalar volume, which can then be visualized by any volume visualization technique, most commonly iso-surfaces and planes.

3. Results

The distinct areas of interest are located in the aft part of the rocket (Figure 10) and will be analyzed separately in the first place. The inlets and the outlets are analyzed first. The flow field at the wake area can be used to evaluate the performance of the overall unit. All three sections can be seen in the annotated areas of Figure 11.

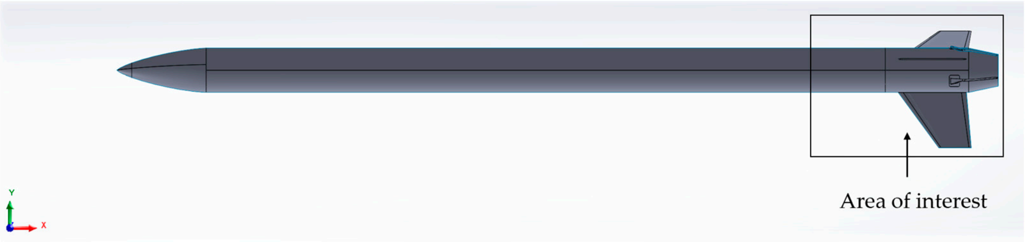

Figure 10. Areas of interest for the unit.

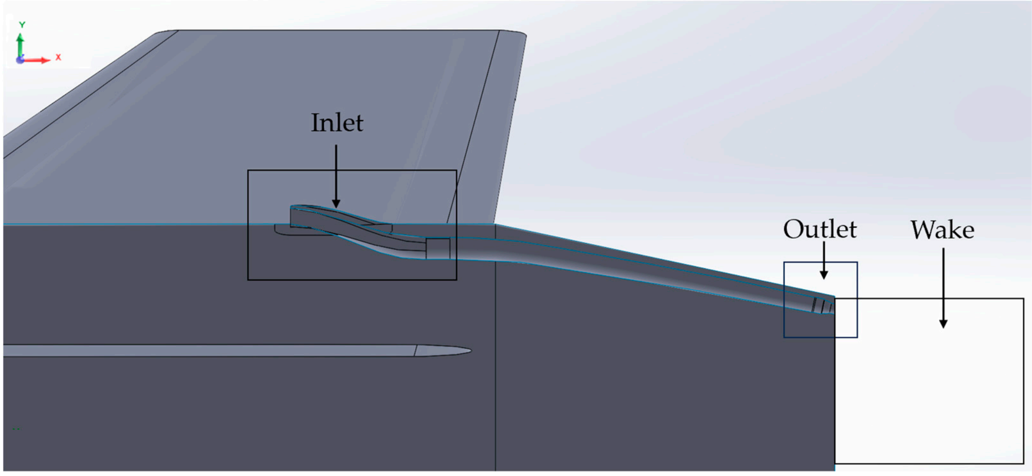

Figure 11. Individual areas of interest for the unit.

3.1. Inlet Analysis Results

3.1.1. Inlet Study Phase Results

The bleed hole scenario simulations indicate an absence of choked flow phenomena, with free-stream air being successfully ingested into the channel, as can be seen in Figures 12 and 13. However, the resultant mass air flow was deemed suboptimal. The protruding geometry scenario, on the other hand, exhibited choked flow primarily attributed to the channel's "diffuser" type design, which allowed for an expansion of the area along the channel (Figure 14). Nevertheless, this scenario demonstrated the successful ingestion of free-stream air with notably higher mass flow coefficients.

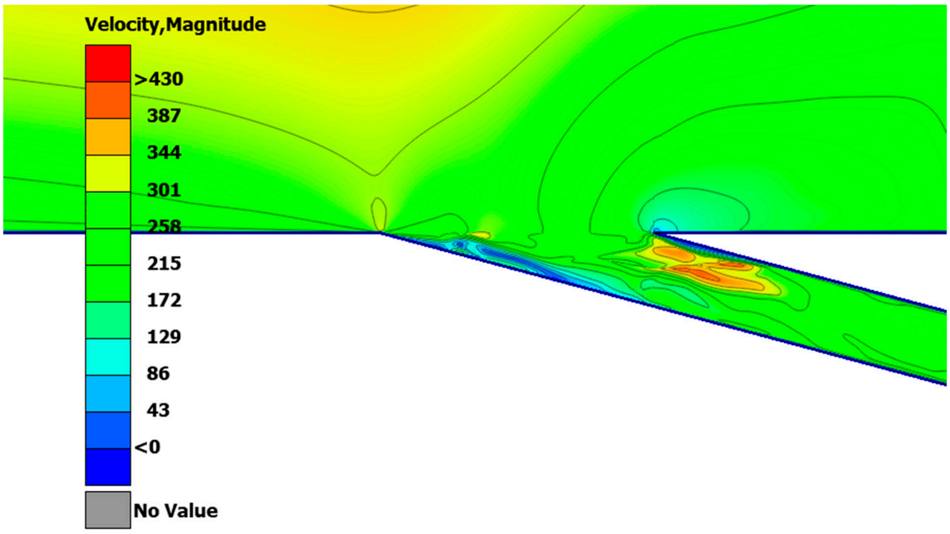

Figure 12. 2D CFD results of the 6 mm bleed hole channel.

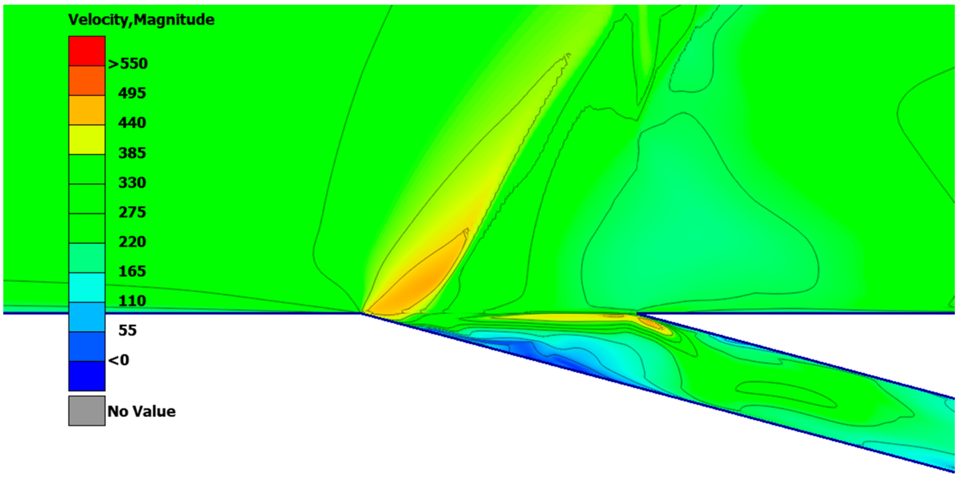

Figure 13. 2D CFD results of the 3 mm bleed hole channel.

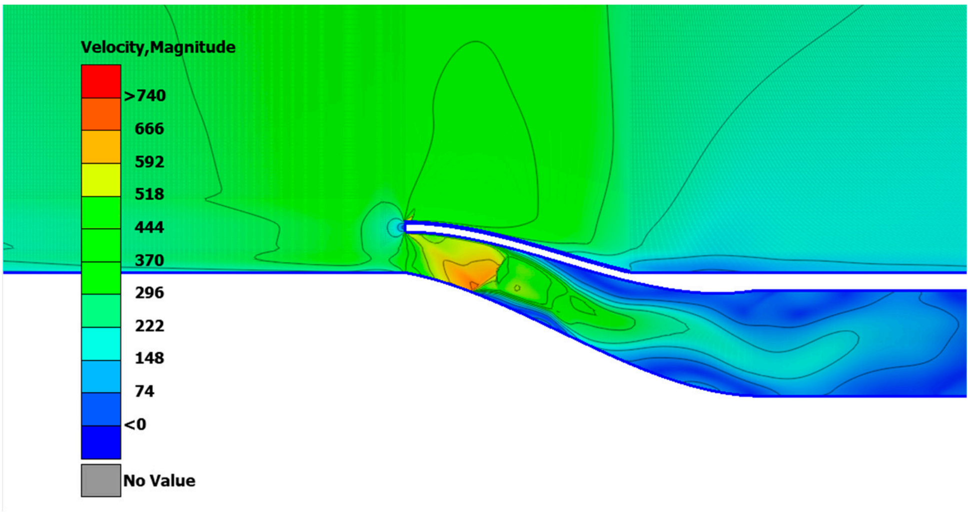

Figure 14. 2D CFD results of the initial protruding channel.

3.1.2. Inlet Design Phase A Results

Mass flow coefficients for the 3 mm bleed hole, 6 mm bleed hole and protruding inlet scenarios are given in Figure 15.

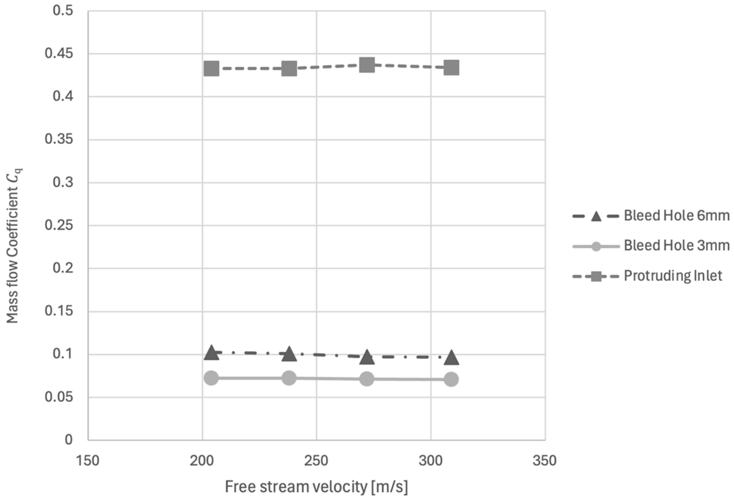

Figure 15. Mass flow coefficient values for different free-stream velocities for the three different inlet geometry scenarios.

For the bleed hole scenario, the geometry produces a mass flow coefficient value which is comparable to [11]. Due to the normal velocity component being aligned with the free-steam velocity vector, the protruding geometry produces a much higher mass flow coefficient, confirming its superiority. It can also be observed that mass flow coefficient remains almost constant for different velocities, making the design process less complicated, as differentiation of performance across the velocity field was not a parameter to consider. It should be noted that CFD results showed a minimal drag increase (in the order of 0.001) due to the protruding geometry, meaning that the geometry displays a very good tradeoff between mass flow ingestion and drag increase.

3.1.3. Inlet Design Phase B Results

The conclusion of Inlet Design Phase B came with the adjusted and final protruding inlet geometry. A flow visualization in the channel from CFD simulations can be seen in Figures 16 and 17.

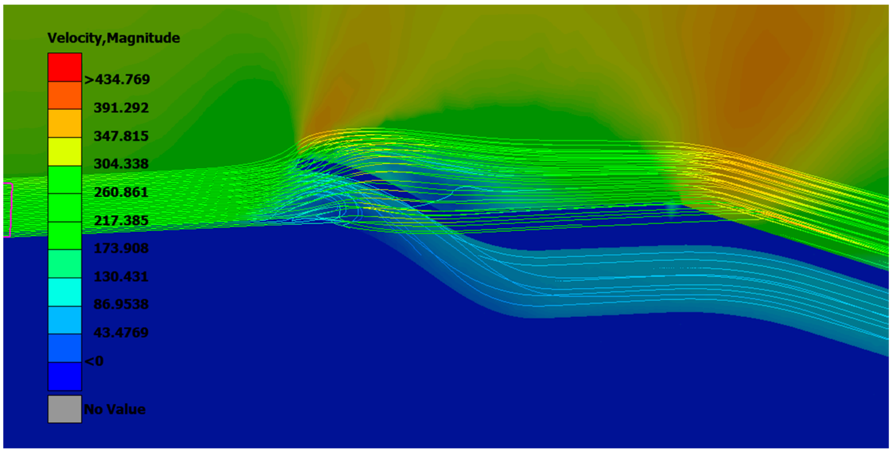

Figure 16. First example of flow paths of the final protruding channel.

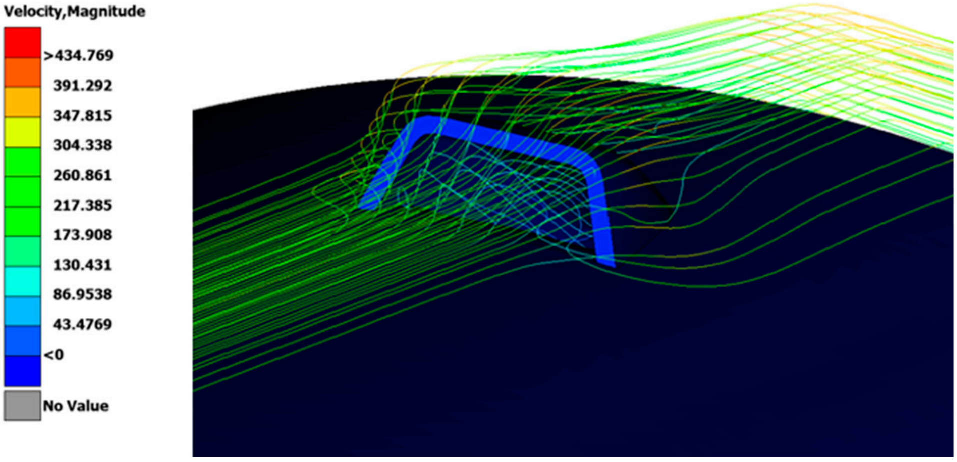

Figure 17. Second example of flow paths of the final protruding channel.

3.2. Outlet Analysis Results

3.2.1. Outlet Study Phase Results

The straight outlet design was reviewed regarding the possibility that the flow will not need any interference as it has optimal characteristics already, guided from the inlets through the veins. The CFD simulations showed that the flow's velocity inside the veins was low compared to the free stream, as can be seen in Figure 18, so further acceleration was needed and the straight outlet design was abandoned as it did not produce the desired result. The bell-shaped nozzle outlet manages to speed up the secondary flow to more optimal velocity values while maintaining a better discharge coefficient in different flow initial velocities, as will be further discussed in the Metrics subsection, also preventing any recirculation of the airflow around the rocket, and the gases produced from the motor's burnout inside the base bleed unit avoid any heat damage. To conclude, the outlet design for the base bleed final design was the bell-shaped nozzle due to its superior characteristics. A visualization of flow inside the bell-shaped nozzle is given in Figure 19.

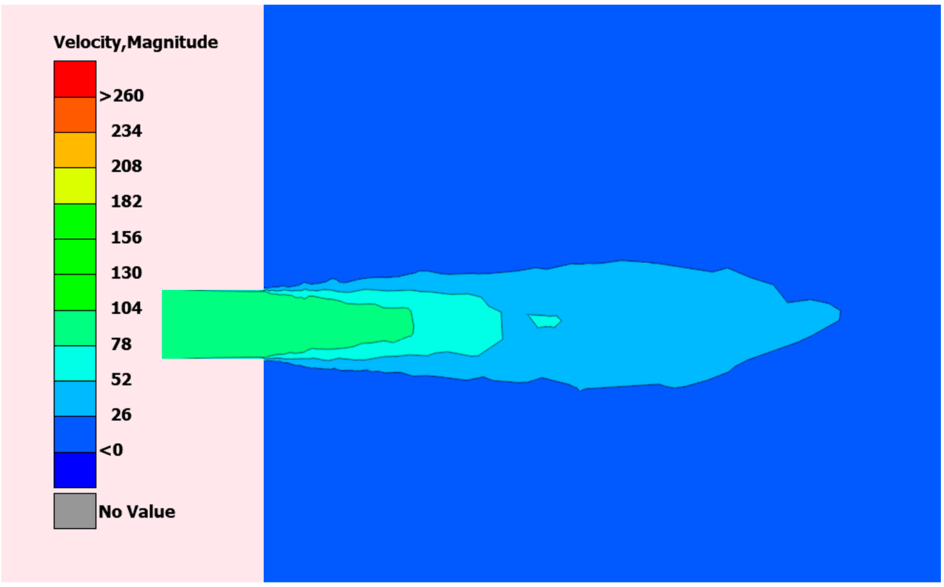

Figure 18. 3D CFD results of the straight outlet design.

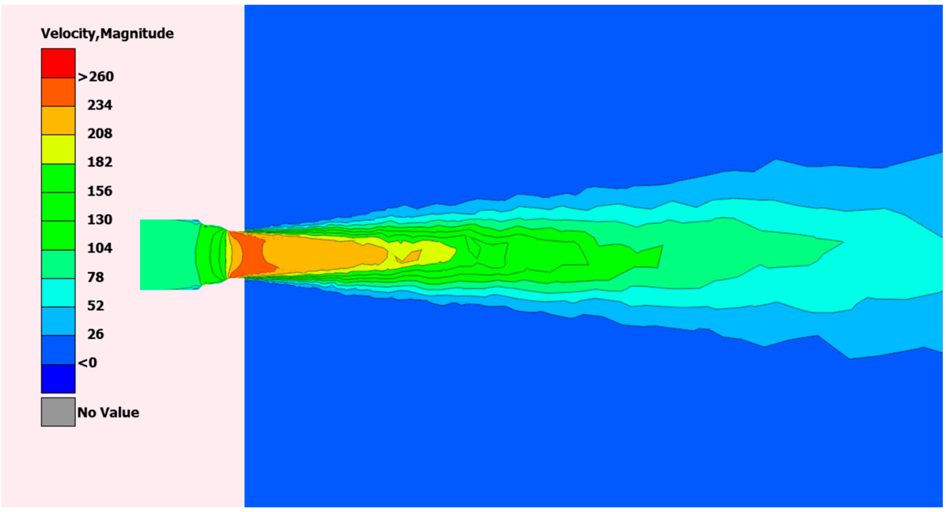

Figure 19. 3D CFD results of the bell-shaped nozzle outlet design.

3.2.2. Outlets Phase A Results

Discharge coefficients for various operating velocities for the two outlet scenarios are given in Figure 20.

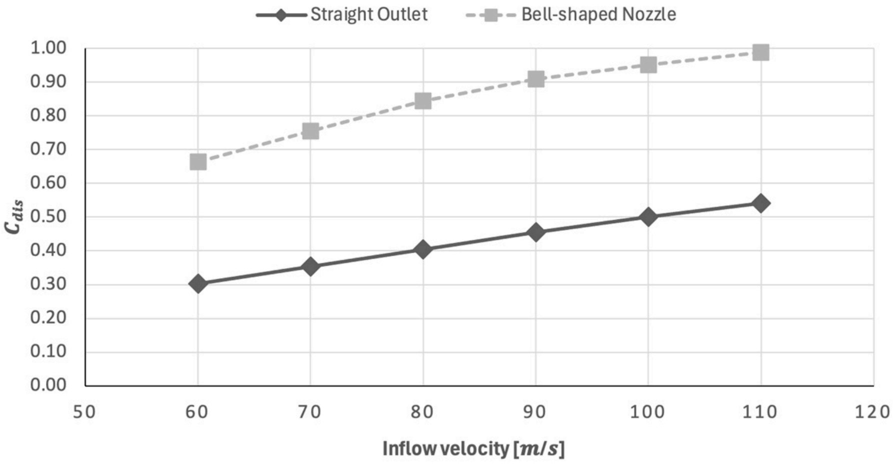

Figure 20. Discharge coefficient values for straight outlet and bell-shaped nozzle scenarios in various velocities.

It can be observed that discharge coefficient values increase steadily with velocity in both geometry scenarios. However, the coefficient is significantly higher for all velocities in the bell-shaped nozzle scenario, therefore deeming it the preferable option. Additionally, a nozzle-type channel prevents any recirculation effects, as shown in [23].

3.2.3. Outlets Phase B Results

Updated simulations on the final design bell-shaped nozzle using CFD are conducted by using input boundary conditions data from the inlets analysis results to achieve more accurate information on the outlets. In this phase, the outlets are downsized from the previous phase design from 6 mm to 4.5 mm on the entrance and from 4 mm to 3 mm. Also, the outlets are adjusted to match the boat-tail angle. The CFD model includes three outlets mounted on the rocket, as this was the final number on the base bleed, trying to simulate the part on a flight scenario. The rocket's geometry is added to the simulation to show the interaction between outlet flow and the rocket's wake. An extension to the outlet's exit is added to match the rocket's bottom surface. Phase B results are given in Figure 21.

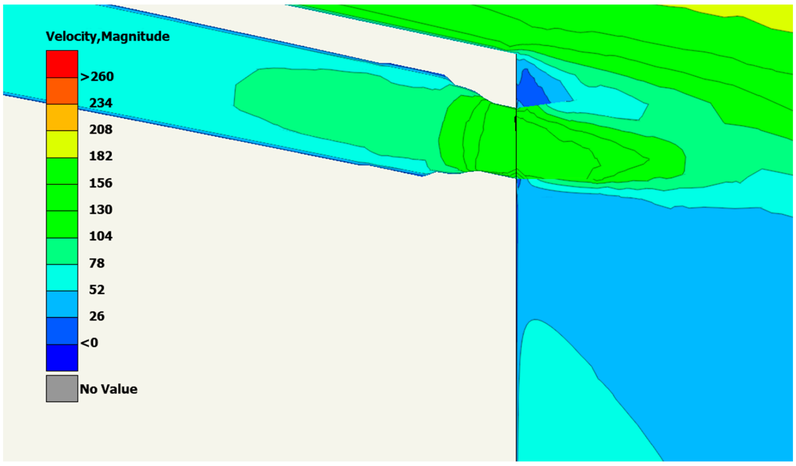

Figure 21. 3D CFD results of the bell-shaped nozzle outlet design of Phase B attached to the rocket.

3.2.4. Final Unit Design

The final unit geometry is presented in Figure 22a. The nozzle-type inlet channel can be seen in Figure 22b. Figure 22a illustrates the trapezoidal inlet face, as inspired by [19]. Figure 22c shows the outlet's exact configuration. Figure 22d illustrates the entire base bleed unit channel. As mentioned above, some of the parameters were dictated by different, already existing parts—that is, the θ angle was pre-determined from boat-tail design. Inlet parameters such as s_1, s_2 and h were initially determined by scaling the geometry from [19]. The scaling was performed in such a way that the inlet maximum diameter (i.e., the diameter at s_3) did not exceed the available space inside the rocket body. A bell-shaped nozzle outlet was designed according to equations by inversing the optimal diffuser design that was acquired from the study by [13]. The outlet's $D_{out,1}$ diameter matched the vein's diameter, and the designed curve inspired by [13] led to the $D_{out,2}$ diameter on the exit. On the outlet's exit, an extension was inserted to keep the nozzle's geometry intact while having a smooth transition from the angled outlet to the cross-section of the rocket's bottom. The exact dimensions of s_1, s_2, s_3, s_4, φ, θ, h, t, R_1, and $D_{out,1and2}$ are given in Table 8.

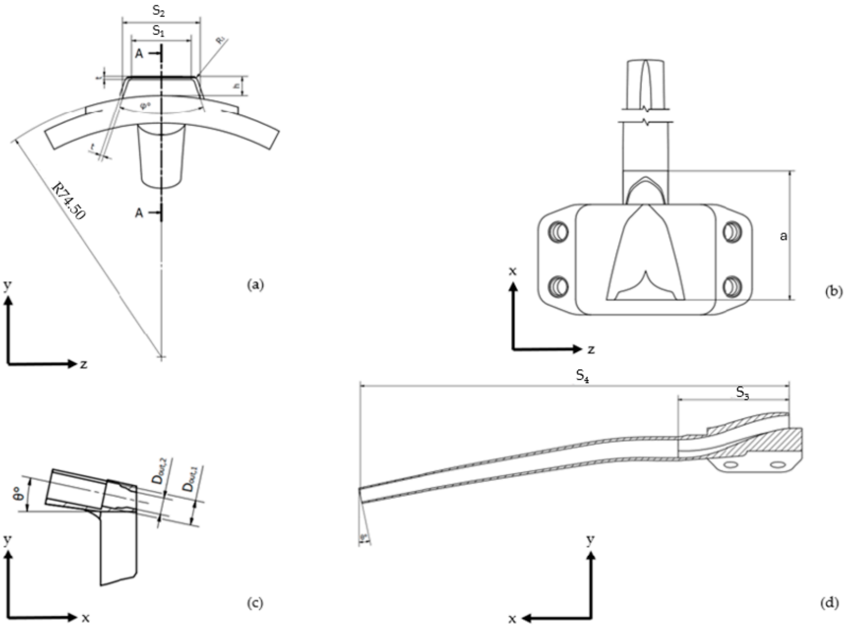

Figure 22. (**a**) Inlet geometry top view. (**b**) Inlet geometry front view. (**c**) Outlet geometry half-section side view. (**d**) Channel half-section side view.

Table 8. Values of final unit dimensions.

Dimension	Value
h	4.6 mm
t	1 mm
S_1	16.9 mm
S_2	22 mm
R_1	2.2 mm
$D_{out,1}$	4.5 mm
$D_{out,2}$	3 mm
S_3	40 mm
S_4	153.8 mm
θ	12°

3.3. Overall Unit Performance Results

3.3.1. C_D Results

CFD simulations were carried out at multiple free-stream velocities and airbrake spans with a base bleed integrated into the rocket to evaluate its effect. The computed C_D values are shown in Table 9. It is shown that at 309 m/s and no airbrake function, the C_D value is at 0.38, achieving a considerable 14.7% overall drag coefficient decrease.

Table 9. Drag coefficient values with and without base bleed for different free-stream velocities.

Free-Stream Velocity (m/s)	C_D with Base Bleed
102	0.091
204	0.08
238	0.08
272	0.32
309	0.32

3.3.2. Lambda 2 Criterion Results

To evaluate the base bleed unit's effect on the wake flow vortices' magnitude and intensity, the lambda 2 criterion is utilized, which is used as a vortex identification metric [24,25].

In the case of the lambda 2 criterion, areas of highly negative values are to be considered as the core areas of vortices. In Figure 23, the unit's effect on the vortex cores can be seen. At the bottom of Figure 23, where the unit is present, the core of the vortex occupies a relatively smaller area that is displayed further away from the rocket. In contrast, the vortex core is slightly bigger at the top of Figure 23, where the unit is not present. As mentioned earlier, the theoretical basis of operation of the unit is to translate the vortices away from the rocket, as observed.

3.4. Performance Assessment

To estimate the performance of the integrated final design in the mission of the rocket, a trajectory tool is used. More specifically, a well-established flight simulator algorithm named rocket.py is used, as suggested by the EuRoC. The algorithm has been developed by Projeto Jupiter of the University of Sao Paulo. The trajectory algorithm is based on Newton's second law with the addition of weather and geographical data that simulate the real flight conditions of the area. The rocket specifications and the CFD are also used as inputs.

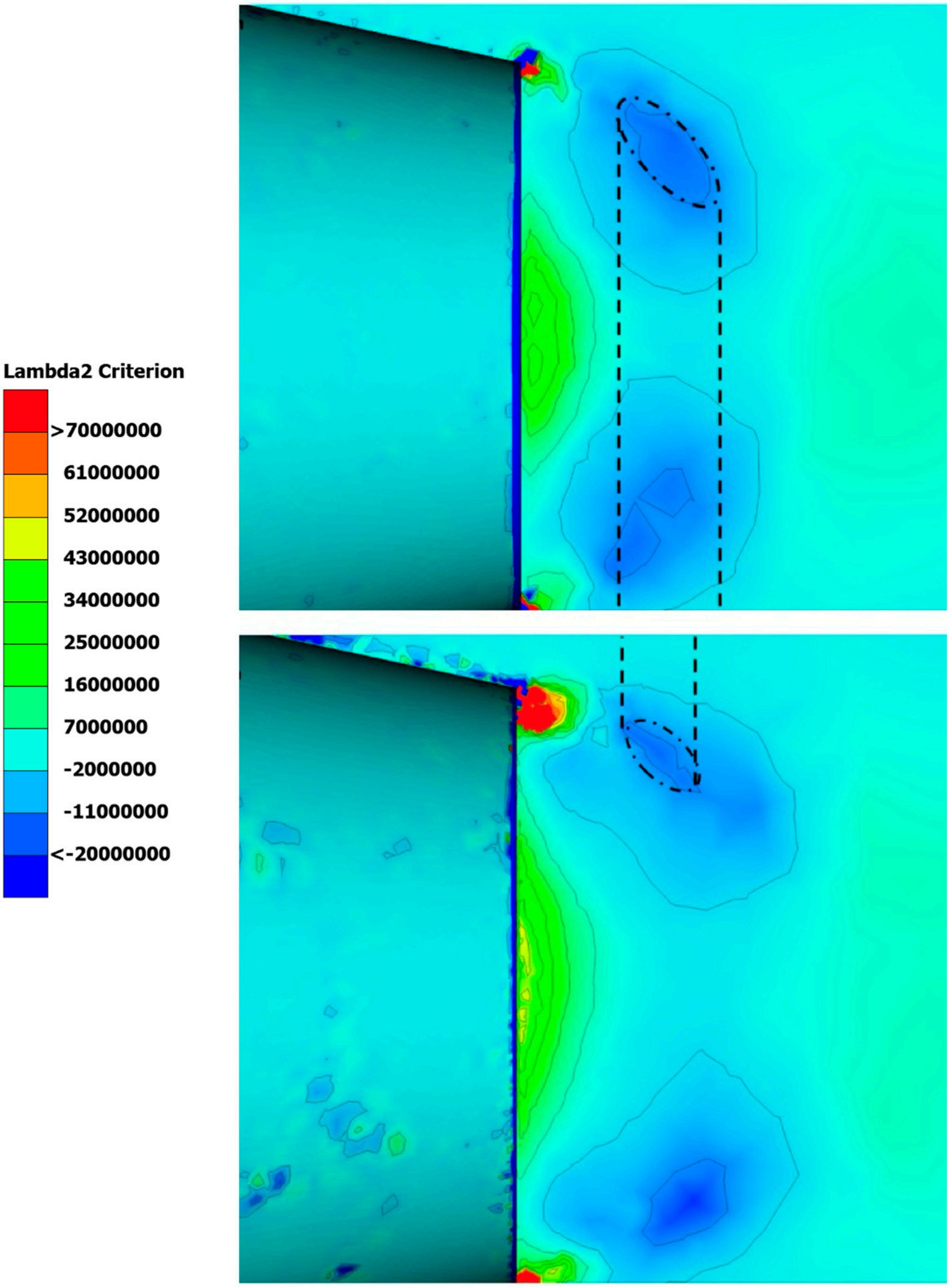

Figure 23. Lambda 2 criterion with base bleed unit (**top**) and without base bleed unit (**bottom**). The core of the vortex is annotated and compared for both configurations.

Specifically, Newton's second law can be expressed as follows in the primary direction of movement with Equation (8):

$$T - \frac{1}{2}\rho V_x^2 A_{reff} C_D - mg - B_{f,x} = ma_x \tag{8}$$

where C_D is the coefficient of drag of the rocket, T is the thrust of the engine that is provided only in the x direction, and $B_{f,x}$ are the external body forces acted upon the rocket by external gusts of wind or other forces in the x-direction. The direction of the external and aerodynamic forces, mainly the drag force, are obtained by the relative position of the rocket at each timestep. This means that the algorithm also computes the pitching moment of the rocket at each timestep by Equation (9) around the center of pressure (C.P.)

$$M_{C.G.} = (X_{C.P.} - X_{C.G.}) \cdot N \tag{9}$$

Note that N is the absolute sum of the normal forces acting on the rocket at the center of pressure, including external and aerodynamic forces as well as the thrust of the motor. As can be seen by Equations (9) and (10), the CFD results can be imported into the code, primarily in the form of the C_D. As discussed in Section 2.2, the CFD simulations are run for specific velocities (0.3 to 0.9 Mach with a step of 0.1) and angles of attack values (0 to 5 degrees with a step of 1); therefore, a linear interpolation is implemented to acquire the $\mathrm{C_D}$ values for intermediate velocity and angle of attack values that occur at the different flight states the algorithm predicts.

3.5. Flight Test and CFD Validation

The data from the flight conducted in the context of the EuRoC served as validation for the CFD model used to evaluate base bleed unit's efficiency. This test flight was conducted on 13 October 2023 under the supervision of the EuRoC authorities, the European Space Agency and the Portugal Space Agency (Figure 24). The flight ascend phase lasted 24 s, reaching an apogee of approximately 2400 m. The maximum speed was 193 [m/s], not reaching the intended 294 [m/s] due to an early braking sequence triggered by an electronics malfunction.

Figure 24. The launch of the Eclipse rocket at the 2023z EuRoC, as captured from the spectator's paddock, located 650 m from the launch rail.

To validate the CFD results, the test data had to be measured and processed. Concerning the measurements, a BMP390 barometer by Bosch Sensortec GmbH (Reutlingen, Germany) was used for pressure measurement. The barometer has a range of 300 to 1250 hPa and an accuracy of 0.3 hPa. The BMI088 accelerometer by Bosch Sensortec GmbH (Reutlingen, Germany), which has a range of up to 24 g (where g is acceleration of gravity) and a maximum error of 1.5%, was used for acceleration measuring. Finally, the Keller Series 33X by Keller Druckmesstechnik AG (Winterhur, Switzerland) was used for thrust calculations through pressure measurements. The Series 33X has a range from 0.1 to

1000 bar and an error of 0.1%. All the measuring tools mentioned have a low enough error to deem the measurements trustworthy. Concerning data processing, a dedicated script was developed that calculates the coefficient of drag during flight. More specifically, the coefficient of drag was calculated using Equation (10).

$$T - D - W = ma_x \; or \; C_D = \frac{m \cdot a_x + m \cdot g - T}{0.5 \cdot \rho_\infty \cdot V_\infty^2 \cdot A_{reff}} \tag{10}$$

Note that m is the mass of the rocket, a_x is the axial acceleration of the rocket, g is the gravitational acceleration, ρ_∞ the density of air at the according altitude, V_∞ is the rocket's velocity and A_{reff} the reference area. The results are summed up in Figure 25 and Table 10. Due to a malfunction in the avionics of the rocket, the flight was carried out with the airbrakes at full deflection (100%) for the entirety of the flight. Therefore, the corresponding CFD results are used, so that the computational setup matches the one encountered during the test. As shown in Table 10, the CFD results deviate up to 8.1% as far as C_D is concerned, which is deemed satisfactory, especially since the testing is conducted in a real (not controlled) environment. A conclusion to be made by comparing the computational and actual flight values is that convergence is achieved. This observation, combined with the fact that the CFD modeling is conducted under the same conditions as the ones encountered in the flight test, serves as evidence that the methodology employed in this work can be trusted to perform the corresponding analyses.

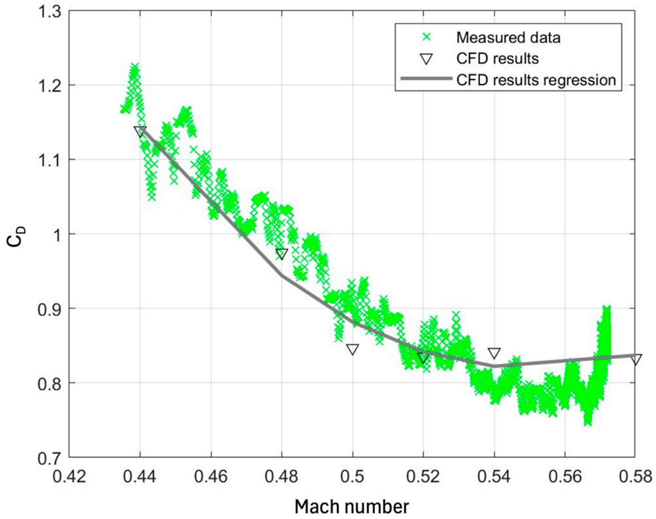

Figure 25. C_D to different Mach number validation diagram. From CFD results to measured data.

Table 10. Measured and calculated coefficient of drag.

Free-Stream Velocity [m/s]	Measured C_D [-]	Calculated C_D [-]	Percentage Deviation
150	1.1710	1.139	2.7%
163.2	1.0193	0.974	4.3%
170	0.9211	0.8467	8.1%
176.8	0.8615	0.8353	3.0%
183.6	0.7771	0.842	7.7%
197.2	0.8350	0.8663	3.7%

4. Discussion

A base bleed unit design study is presented on a rocket vehicle that operates up to transonic speeds. A step-by-step presentation of the design process is provided, along with the corresponding philosophy behind the selection of the metrics and the computational methodology. The authors not only provide a specific set of results but go through a step-by-step presentation of their methodology and considerations, opening the way for future design studies on passive flow control devices to be conducted on rockets by researchers who investigate means of reducing drag and, thus, fuel consumption.

Both 2D and 3D CFD modeling is used to evaluate the various design choices and come up with the base bleed configuration. The modeling parameters are selected in accordance with the corresponding literature for each respective phase and component. That is, each of the base bleed unit's respective components, i.e., the inlet and the outlet, are initially investigated in terms of their design philosophy, size, and shape. The integrated rocket, including the resulting base bleed unit, is then evaluated by means of CFD, and the results are validated against full-scale field test (launch) data. Using the rocket.py trajectory tool, an adequate agreement is achieved between the test data and CFD computations.

The result is a unique configuration, which consists of a protruding geometry inlet and a nozzle-type outlet. To the best of our knowledge, these characteristics have not been reported in other base bleed studies, where the common practice is to employ angled holes (bleed holes) in the body of the platform, as well as a straight or angled pipe outlet, with the pipe diameter, however, remaining constant. This is an indication that the boundary conditions of the current design study, i.e., the operating conditions and limitations, lead to a different design philosophy tailored to the needs of the high-power reference platform.

5. Conclusions

The resulting conclusions are:

- Designing a base bleed unit for a rocket is constrained by specific weight and volume considerations, which reduce the design space of such a study.
- The authors suggest that the unit is broken down to its sections, i.e., the inlets and the outlets, each of which is initially analyzed separately. The integrated base bleed configuration is then investigated and evaluated.
- A protruding inlet is selected as the preferred inlet geometry, as results show that it displays superior mass flow ingestion compared to classic bleed-hole-type geometries with a minimal drag increase.
- A bell-shaped nozzle outlet design is suggested as the superior outlet alternative from those tested as it shows a better discharge coefficient compared to the straight outlet design. The nozzle prevents any recirculation, making sure hot gases from the motor burnout do not enter the unit, and helps the flow reach certain velocities at the unit's, exit making it a better designing choice.
- CFD results showed a remarkable, double-digit net decrease in overall drag coefficient at Mach 0.9. More specifically, a 15% enhancement is achieved.
- The comparison between the flight test and the CFD results showed that, despite the complex flow phenomena encountered during the operation of the rocket, the two methods are in close agreement.

6. Future Work

Concerning suggestions for future work, the present study is based on a heuristic approach. Although this approach indicates that the base bleed concept can effectively be used for a rocket drag reduction, employing an optimization algorithm regarding the generation of Bezier curves for the vanes could help in further optimizing the configuration and reducing the pressure drop inside the vanes. That is, using a multidisciplinary optimization framework could provide even better results, exploiting the potential of such a unit. Moreover, time and resources limitations did not allow for the reference rocket configuration and base bleed unit to be designed in parallel. However, if the rocket design engineers can develop both configurations simultaneously, the weight and volume requirements of the base bleed could be considered as part of the overall rocket design study, thus expanding its design space and improving overall performance. Higher-fidelity turbulence modeling, such as LES, as mentioned, can improve the accuracy of the CFD model. Additionally, more test flight data from future launches can be used to determine the uncertainty of the trajectory tool and optimize its performance. Finally, the implementation of an active base bleed unit can be considered, on the condition that the mass and volume requirements of an active unit are considered from the rocket's conceptual design phase.

Author Contributions: Conceptualization, P.F.; methodology: P.F., A.S. and A.K.; software, P.F., A.S. and A.K.; validation, P.F.; formal analysis, A.S. and A.K.; investigation, P.F., A.S. and A.K.; Resources, C.K. and P.P.; data curation, P.F., A.S. and A.K.; writing-original draft preparation, P.F., A.S. and A.K.; writing-reviewing and editing, P.F., A.S., A.K. and P.P.; visualization, P.F., A.S., A.K. and P.P.; supervision, P.P.; project administration, C.K. and P.P.; funding acquisition, C.K. and P.P. All authors have read and agreed to the published version of the manuscript.

Funding: This research received no external funding.

Data Availability Statement: The data presented in this study are available on request from the corresponding author due to privacy reasons.

Acknowledgments: Results presented in this work have been produced using the Aristotle University of Thessaloniki (AUTh) High-Performance Computing Infrastructure and Resources.

Conflicts of Interest: The authors declare no conflicts of interest.

Nomenclature

St	Strouhal number
M	Mach number
cal	Caliber stability
C_q	Mass flow coefficient
ρ_∞	Free-stream density
V_∞	Free-stream velocity
A_{reff}	Area surface perpendicular to the air flow
C_D	Drag coefficient
C_{dis}	Discharge coefficient
M_{actual}	CFD results calculated actual mass flow
M_{isen}	Ideal mass flow in an isentropic flow outlet
M_w	Molecular weight of air
R_g	Universal gas constant
γ	Isentropic exponent
S	Rate-of-strain tensor
Ω	Rate-of-rotation tensor
λ	Eigenvalue
h	Protruding inlet geometry height
t	Protruding inlet geometry thickness
S_1	Protruding inlet geometry trapezoid top line length
S_2	Protruding inlet geometry trapezoid base line Length
R_1	Protruding inlet geometry fillet radius
$D_{out,1}$	Bell-shaped outlet's entry diameter
$D_{out,2}$	Bell-shaped outlet's exit diameter
S_3	Protruding inlet geometry overall length
S_4	Base bleed overall length
θ	Base bleed angle to rocket's x axis
T	Motor thrust
$B_{f,x}$	External body forces
$C.G.$	Center of gravity
$C.P.$	Center of pressure
$x_{C.P.}$	Position of center of pressure on rocket's x axis
$M_{C.P.}$	Torque around the center of gravity
$x_{C.G.}$	Position of center of gravity on rocket's x axis

References

1. NASA. Saturn Report. 1959. Available online: https://ntrs.nasa.gov/citations/19640058212 (accessed on 30 March 2024).
2. Rocket Propulsion Market Size, Share, Trends, Growth And Industry Forecast 2024–2033. Available online: https://www.thebusinessresearchcompany.com/report/rocket-propulsion-global-market-report (accessed on 31 March 2024).
3. Anderson, J. *Fundamentals of Aerodynamics*, 5th ed.; McGraw-Hill: New York, NY, USA, 2011; ISBN 978-0-07-339810-5.
4. Moore, F.G.; Wilcox, F.; Hymer, T. Base drag prediction on missile configurations. *J. Spacecr. Rocket.* **1994**, *31*, 759–765. [CrossRef]
5. Statnikov, V.; Saile, D.; Meiß, J.-H.; Henckels, A.; Meinke, M.; Gülhan, A.; Schröder, W. Experimental and numerical investigation of the turbulent wake flow of a generic space launcher configuration. *EDP Sci.* **2015**, *7*, 329–350. [CrossRef]
6. Danberg, J.E.; Nietubicz, C.J. Predicted flight performance of base-bleed projectiles. *J. Spacecr. Rocket.* **1992**, *29*, 366–372. [CrossRef]
7. Choi, J.-Y.; Shin, E.; Kim, C.-K. Numerical Study of Base-Bleed Projectile with External Combustion. In Proceedings of the 41st AIAA/ASME/SAE/ASEE Joint Propulsion Conference & Exhibit, Tucson, AZ, USA, 10–13 July 2005. [CrossRef]
8. Abou-Elela, H.; Ibrahim, A.; Mahmoud, O.; Abdel-Hamid, O. Ballistic Analysis of a Projectile Provided with Base Bleed Unit. In Proceedings of the International Conference on Aerospace Sciences and Aviation Technology, Cairo, Egypt, 28–30 May 2013; Volume 15, pp. 1–22. [CrossRef]
9. Xue, X.; Yu, Y. An improvement of the base bleed unit on base drag reduction and heat energy addition as well as mass addition. *Appl Therm. Eng.* **2016**, *109*, 238–250. [CrossRef]
10. Paul, S.; Raj, A.V.; Kumar, C.S. Inward turning base-bleed technique for base drag reduction. *Aeronaut. J.* **2023**, *127*, 370–397. [CrossRef]
11. Motallebi, F.; Norbury, J.F. The effect of base bleed on vortex shedding and base pressure in compressible flow. *J. Fluid Mech.* **1981**, *110*, 273–292. [CrossRef]
12. Viswanath, P.R.; Patil, S.R. Effectiveness of passive devices for axisymmetric base drag Reduction at Mach 2. *J. Spacecr. Rocket.* **1990**, *27*, 234–237. [CrossRef]
13. Madsen, J.I.; Shyy, W.; Haftka, R.T. Response surface techniques for diffuser shape optimization. *AIAA J.* **2000**, *38*, 1512–1518. [CrossRef]
14. Nicolás-Pérez, F.; Velasco, F.; García-Cascales, J.; Otón-Martínez, R.; López-Belchí, A.; Moratilla, D.; Rey, F.; Laso, A. On the accuracy of RANS, DES and LES turbulence models for predicting drag reduction with Base Bleed technology. *Aerosp. Sci. Technol.* **2017**, *67*, 126–140. [CrossRef]
15. Nair, P.P.; Suryan, A.; Kim, H.D. Computational study on flow through truncated conical plug nozzle with base bleed. *Propuls. Power Res.* **2019**, *8*, 108–120. [CrossRef]
16. Spalart, P.R.; Rumsey, C.L. Effective Inflow Conditions for Turbulence Models in Aerodynamic Calculations. Available online: https://ntrs.nasa.gov/search.jsp?R=20070035069 (accessed on 30 March 2024).
17. Sahu, J.; Heavey, K.R. Numerical investigation of supersonic base flow with base bleed. *J. Spacecr. Rocket.* **1997**, *34*, 62–69. [CrossRef]
18. Thies, A.T.; Tam, C.K.W. Computation of turbulent axisymmetric and nonaxisymmetric jet flows using the K-epsilon model. *Aerosp. Res. Cent.* **2012**, *34*, 309–316. [CrossRef]
19. Tournier, S.E.; Paduano, J.D.; Pagan, D. Flow Analysis and Control in a Transonic Inlet. In Proceedings of the 23rd AIAA Applied Aerodynamics Conference, Toronto, ON, Canada, 6–9 June 2005.
20. Nelson, W.J.; Dewey, P.E. A Transonic Investigation of the Aerodynamic Characteristics of Plate- and Bell- Type Outlets for Auxiliary Air. 1952. Available online: https://ntrs.nasa.gov/citations/19930087254 (accessed on 31 March 2024).
21. Kayser, J.C.; Shambaugh, R.L. Discharge coefficients for compressible flow through small-diameter orifices and convergent nozzles. *Chem. Eng. Sci.* **1991**, *46*, 1697–1711. [CrossRef]
22. Dong, Y.; Yan, Y.; Liu, C. New visualization method for vortex structure in turbulence by lambda2 and vortex filaments. *Appl. Math. Model.* **2016**, *40*, 500–509. [CrossRef]
23. Cobb, G.R.; Sauer, J.A.; Hemming, M.R.; Xu, K.G. Experimental Study of Fluidic Diode Geometries for Injector Backflow Mitigation. In Proceedings of the AIAA SCITECH 2024 Forum, Orlando, FL, USA, 8–12 January 2024.
24. Zhan, J.M.; Chen, Z.Y.; Li, C.W.; Hu, W.Q.; Li, Y.T. Vortex identification and evolution of a jet in cross flow based on Rortex. *Eng. Appl. Comput. Fluid Mech.* **2020**, *14*, 1237–1250. [CrossRef]
25. Jeong, J.; Hussain, F. On the identification of a vortex. *J. Fluid Mech.* **1995**, *285*, 69–94. [CrossRef]